Materials Advances

PAPER

Check for updates

Conductive 3D SW-/MW-CNTs hybrid frameworks for ultra-high-content Prussian white cathodes in sodium-ion batteries

Yang He,[a] Tingru Chen[b] and Nobuyuki Zettsu ⓘ *[abc]

The need for enhancing the cyclability of Prussian white (PW) cathodes is highly desirable due to their potential as promising cathode materials for sodium-ion batteries (SIBs). In this study, an ultra-high PW content of up to 98 wt% was accomplished in PW-based cathodes *via* self-organization of a homogeneous 3D carbon nanotubes (CNTs) network structure. The half-cell fabricated using the PW/CNT cathode exhibited a high C-rate capability of 103.8 mAh g^{-1} at 10C and an excellent cycling stability of 99.3% after 50 cycles at 0.2C, eliminating the need for a polymeric binder. Moreover, hybridizing multi-walled CNTs with a small amount of single-walled CNTs in a specific composition enabled the fabrication of hybrid cathode materials with sufficient electron conductivity, Na$^+$ accessibility, and structural stability, making them suitable for energy storage applications. The proposed architecture of PW materials can effectively suppress irreversible phase transitions at high operating voltages by stabilizing the lattice structure and hindering the formation of undesirable phases, thus improving battery performance. Furthermore, the design of the cathode material presented in this study can effectively enhance the energy density of SIBs while maintaining high C-rate capability and cyclability.

Introduction

The rapid advancement of renewable energy technologies, including wind, solar, and tidal energy, has made large-scale energy storage a global research hotspot.[1] Secondary batteries are regarded as highly promising candidates for energy storage applications owing to their high energy density and versatility. In the 1990s, Sony developed and commercialized the first generation of lithium-ion batteries (LIBs), laying the foundation for modern electronics.[2,3] Following more than 30 years of significant advancements, LIBs have been widely used in various aspects of our lives, including in wearable electronic devices and electric vehicles. However, owing to the uneven distribution of lithium resources and increasing annual costs, LIBs are not suitable for large-scale energy storage applications. Sodium-ion batteries (SIBs) possess an energy storage mechanism similar to that of LIBs.[4,5] SIBs, with their widely distributed and abundant sodium resources and relatively lower costs compared to those associated with LIBs, are emerging as an advantageous option for large-scale energy storage.

The cathode materials for SIBs primarily consist of Prussian blue analogs (PBAs),[6-8] layered metal oxides,[9] polyanions,[10] and organic compounds.[11] PBAs, characterized by the general chemical formula Na$_x$M[Fe(CN)$_6$]$_y$·□$_{1-y}$·zH$_2$O (where M represents transition metal ions, $0 < x < 2$, $0 < y < 1$, and □ denotes [Fe(CN)$_6$] vacancies), can exhibit cubic, monoclinic, and rhombohedral crystal symmetries. PBAs have garnered significant attention as battery materials due to their high theoretical capacity (up to 170 mAh g^{-1} with two Na$^+$ storage), ease of synthesis, low cost, and open framework structure, which facilitates rapid Na$^+$ insertion/extraction.[12,13] Conversely, Mn-based Prussian white (PW) cathodes are prone to structural collapse and capacity decay after repeated Na$^+$ insertion/extraction due to the presence of [Fe(CN)$_6$] vacancies, lattice water, and Jahn–Teller distortion of Mn^{3+}, making the enhancement of their long-term cyclability crucial.[14,15] Therefore, the enhancement of cyclability of PW cathodes is highly desirable.

In recent years, various approaches, including vacancy regulation, transition metal substitution, and high-entropy engineering, have been used to enhance material properties and create novel energy storage materials. High-entropy PBAs exhibit significant lattice tolerance and efficient multipath electron transfer.[16] Therefore, modifying and optimizing existing PBAs, such as PW materials, is a practical and feasible approach to achieve their desirable properties. Furthermore, artificial solid electrolyte interface coatings, especially those

[a] Institute for Aqua Regeneration, Shinshu University, 4-17-1 Wakasato, Nagano, 380-8553, Japan. E-mail: zettsu@shinshu-u.ac.jp
[b] Department of Materials Chemistry, Faculty of Engineering, Shinshu University, 4-17-1 Wakasato, Nagano, 380-8553, Japan
[c] Energy Landscape Architectonics Brain Bank, Shinshu University, 4-17-1 Wakasato, Nagano, 380-8553, Japan

incorporating carbonaceous inclusions and conducting polymers, have been demonstrated to effectively enhance the structural stability and electron/ion transport kinetics in energy storage devices.[17–20] Additionally, optimizing the operating voltage range plays a pivotal role in determining the stability of electrode materials in batteries. Typically, a relatively higher upper voltage limit enhances specific capacity while promoting irreversible structural degradation, which is often closely associated with irreversible phase transitions.[21] Furthermore, at high voltages, the coordinated water within the lattice may undergo side reactions with the electrolyte, degrading battery performance and safety.[22]

In this study, high content PW cathode materials (up to 98 wt%) were achieved through self-organization of a three-dimensional (3D) network of multi-walled carbon nanotubes (MW-CNTs) and single-walled CNTs (SW-CNTs) hybrids. Our motivation lies in understanding how electrode structures and formulations affect the electrochemical performance of PW cathodes—an area that has received limited attention. While previous studies have often centered on material-level modifications (*e.g.*, elemental doping, surface coatings, or *in situ* growth), they still predominantly utilize conventional electrode formulations rich in inactive components such as binders and carbon additives. In designing PW cathode materials for SIBs, we expect that a three-dimensional (3D) CNTs network provides sufficient electronic conductivity and Na$^+$ accessibility by reducing the usage amount of carbon and polymeric binders while mitigating the volumetric expansion/contraction of the PW structure during charge/discharge cycles. Furthermore, the homogenization of the reaction distribution formed in the composite electrode provided by the organized structure in which PW particles are embedded in the proposed CNTs network will effectively suppress the occurrence of irreversible phase transitions during high voltage operation.

Experimental

Preparation of electrodes

To prepare PW/CNT (polymeric binder-free) cathodes, initially, multi-walled carbon nanotubes slurry (MW-CNTs, 5 wt% in NMP, Toda Kogyo Corp., Japan) and single-walled carbon nanotubes slurry (SW-CNTs, 0.2 wt% in NMP, Meijo Nano Carbon Co., Ltd, Japan) were mixed in a container at a mass ratio of 9:1 (actual mass ratio of carbon nanotubes). The mixture was thoroughly stirred to achieve uniformity using a planetary centrifugal mixer (THINNKY MIXER AR-100, THINNKY, Japan). Subsequently, commercial PW powder (Xiamen Tob New Energy Technology Co., Ltd) was added to the CNTs mixture in the desired proportion (PW:CNTs = 98:2 (wt%)), and a small amount of NMP was further added to adjust the slurry's viscosity. The mixture was then stirred again to obtain a homogeneous electrode slurry. For comparison, 80 wt% of PW, 10 wt% of acetylene black, and 10 wt% of polyvinylidene fluoride (PVDF) binders were mixed with an appropriate amount of NMP (the same stirring process as the

second stirring process of the PW/CNT cathode) to obtain a uniform slurry. Finally, the two slurries were respectively coated onto a carbon-coated aluminium (Al@C) sheet. The electrodes were vacuum-dried overnight at 120 °C. Circular discs with a diameter of 14 mm were then punched out from the carbon-coated aluminium sheets to serve as cathodes. The electrodes had an average thickness of 38 μm, including the carbon-coated aluminium foil (Al@C, 22 μm), with a mass loading of PW in the range of 2.0–2.4 mg cm^{-2}. Prior to manuscript preparation, multi-walled carbon nanotubes (MW-CNTs) were hybridized with small amounts of single-walled carbon nanotubes (SW-CNTs) at optimized ratios, determined through a series of experiments investigating the influence of CNTs composition on electrode performance.

Structural characterization

The phase composition of PW powder and the cycled electrodes was characterized by X-ray diffraction (XRD) with a Cu-Kα radiation source (Rigaku Ltd, Japan). Thermogravimetry-differential thermal analysis (TG-DTA, Rigaku Ltd, Japan) and inductively coupled plasma mass spectrometry (ICP-MS, Seiko Instruments Inc.) were performed to analyse the specific chemical composition of PW. The elemental composition and chemical valence states of cycled and uncycled cathodes were detected by X-ray photoemission spectroscopy (XPS; JPS-0910, JEOL Co., Ltd, Japan). Intact sliced electrodes were obtained through focused ion beam (FIB) milling. The morphological characteristics and microstructure of the cathodes were observed by field-emission scanning electron microscopy (FE-SEM, JSM-7600F at 15 kV; JEOL, Japan).

Electrochemical characterization

The half-cell was assembled with Na metal as the counter electrode and the glass fiber type GF-A as the separator. One molarity (1 M) NaClO$_4$ in polycarbonate mixed with 3 wt% fluoroethylene carbonate (FEC) additive as the electrolyte. R2032 coin-type cells were fabricated in an Ar-filled glove box. The galvanostatic charge/discharge, rate performance, and galvanostatic intermittent titration technique (GITT) measurements were conducted on a Neware Battery Testing System. To prevent irreversible phase transitions and maintain high cycling stability, the fabricated PW/CNT electrode was initially activated at a high operating voltage (2–4.2 V *vs.* Na/Na$^+$) before testing within an optimized voltage window. To ensure the complete extraction of Na ions (Na$^+$) from the cathode, a constant current–constant voltage (CC–CV) technique was employed. Cyclic voltammetry (CV) measurements were performed using an electrochemical workstation (VSP-300, Biologic, France) over a voltage range of 2.0 to 3.6 V following the activation process, with scan rates varying from 0.1 to 0.5 mV s^{-1}. Electrochemical impedance spectroscopy (EIS) measurements were performed using an electrochemical workstation over a frequency range of 200 kHz to 1 mHz. Herein, all electrochemical tests were conducted at ambient temperature. The electrochemical performance of the PW/CNT electrodes was compared to those of the binder-containing PW/acetylene black + polyvinylidenefluoride (AB+PVDF) electrodes.

Results and discussion

Microstructure of the PW/CNT 3D network system

As schematically illustrated in Fig. 1(a), Prussian white (PW) and carbon nanotubes (CNTs) were assembled using a conventional slurry process, as described in our previous report.[23] A mixture of single-walled carbon nanotubes (SW-CNTs) and multi-walled carbon nanotubes (MW-CNTs) was employed as a conductive binder in place of polyvinylidene fluoride (PVDF). For comparison, control composite electrodes composed of PW, acetylene black, and a PVDF binder were also fabricated. Notably, the use of CNT-based binders enables the stable fabrication of composite electrodes on carbon-coated aluminum (Al@C) foil using standard coating processes, even with a relatively low total additive content of approximately 2 wt%.

Commercially available Mn-based Prussian white (PW), in which Mn^{2+} and Fe^{2+} ions coordinate with nitrogen and carbon atoms in $-C\equiv N-$ ligands to form a three-dimensional open framework with spacious ion channels, was used as the active material. These ion channels within the 3D framework facilitate the reversible insertion/extraction and transport of Na^+ ions during electrochemical reactions.[24] The XRD pattern shown in Fig. 1(b) exhibits distinct peak splitting at approximately $2\theta = 24.4°$, $38°$, and $50°$, which is characteristic of the monoclinic phase of PW with a space group of $P2_1/n$. The refined lattice parameters ($a = 10.5952$ Å, $b = 7.5331$ Å, and $c = 7.3315$ Å) further confirm the presence of this monoclinic structure.

To further investigate the chemical composition of the samples, thermogravimetric-differential thermal analysis (TG-DTA) and inductively coupled plasma mass spectrometry (ICP-MS) were conducted. In the TG-DTA curve of PW after vacuum drying (Fig. 1(c)), the observed weight loss below 260 °C is attributed to the removal of water molecules,[25] corresponding to approximately 10.3 wt%. Based on the elemental composition obtained from ICP analysis (Table S1), the chemical formula of PW after vacuum drying is determined to be $Na_{1.46}Mn[Fe(CN)_6]_{0.983}\cdot\square_{0.017}\cdot1.94H_2O$.

Fig. 2 presents the field-emission scanning electron microscopy (FE-SEM) images of the pristine PW powders and the corresponding PW/CNT electrode surfaces. As shown in Fig. 2(a) and (b), the PW powder exhibits a well-defined cubic morphology with an average particle size of approximately 1 μm. Fig. 2(c) and (d) demonstrate that both MW-CNTs and
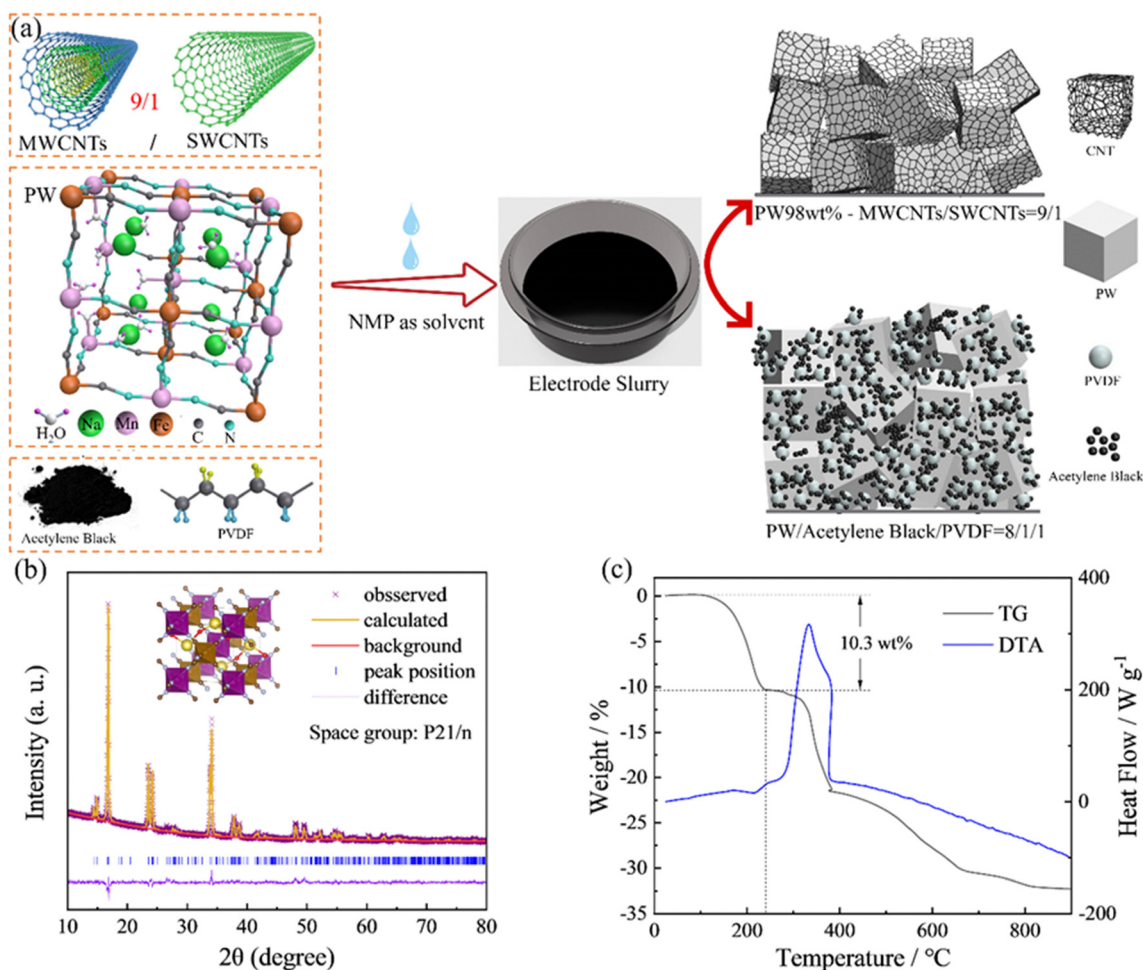

Fig. 1 (a) The preparation process of electrodes and the schematic diagram of the electrode structure. (b) Powder XRD patterns of PW and the Rietveld refinement. (c) TG-DTA curve of PW after vacuum drying at 120 °C.
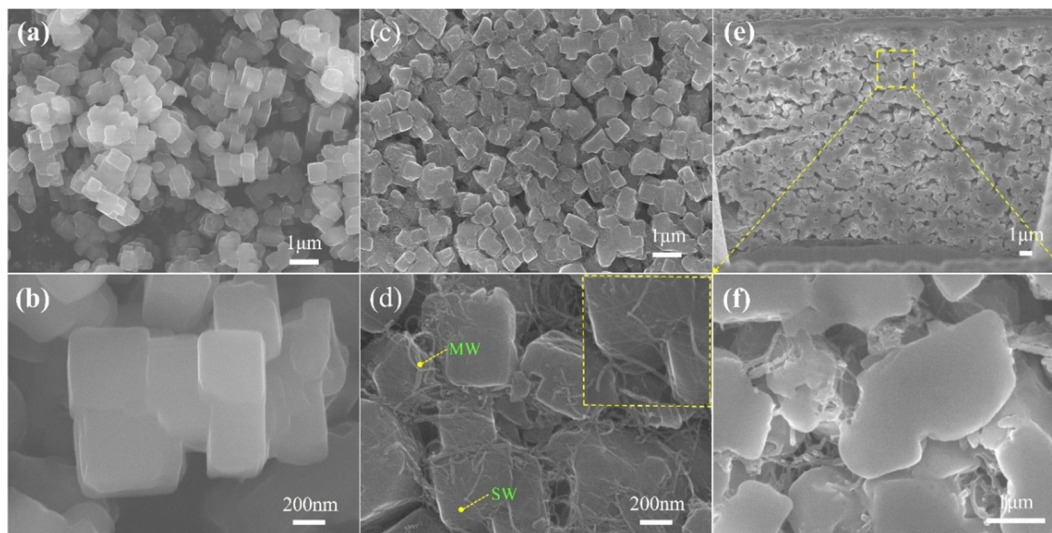
Fig. 2 FE-SEM images of (a) and (b) PW powders, (c) and (d) the PW/CNT electrode surface, and (e) and (f) cross-section.

SW-CNTs are homogeneously distributed and form an interconnected network across the electrode surface, as well as on the individual PW particles. To further confirm the formation of a CNTs network within the electrode structure, FE-SEM analysis was performed on cross-sectional samples prepared using focused ion beam (FIB) milling. As shown in Fig. 2(e) and (f), CNT bundles are observed bridging the intergranular nanoscale voids, effectively connecting the particles and contributing to a continuous conductive network throughout the electrode. Furthermore, it, representative of other areas of the electrode, shows that both MW-CNTs and SW-CNTs are uniformly distributed across the electrode surface, forming a continuous and well-dispersed three-dimensional conductive network.

The results of multiprobe surface potential measurements on the PW-based electrode sheets were numerically deconvoluted into contributions from bulk (volume) resistance, surface resistance, and interfacial resistance at the current collector. Measurements were conducted at 25 distinct points on each electrode, with the resulting distributions presented as violin plots in Fig. S1 and summarized in Table S2. The PW/CNT electrode exhibited a bulk resistivity of 2.69 Ω cm, which is lower than that of the PW/AB+PVDF electrode, despite the conductive carbon content in the PW/CNT electrode being only one-fifth that of the PW/AB+PVDF counterpart. Importantly, the variation in volume resistance across the 25 measurement points was minimal. Given that electrons preferentially follow paths of least resistance, this low dispersion suggests that all PW particles are effectively embedded within the three-dimensional interwoven CNTs network, providing uniform electrical connectivity throughout the electrode. The improved contact between PW particles and CNTs facilitates efficient electron transport, enabling faster charge transfer and mitigating structural degradation during cycling.

Notably, the planar and cross-sectional FE-SEM images (Fig. S2) of the PW/AB+PVDF electrode reveal inhomogeneously distributed agglomerates of acetylene black (AB) particles on the surface of the PW powder. Most of these particles are concentrated in the central regions of the intergranular nanospace. This FE-SEM analysis indicates that the PW particles in the PW/AB+PVDF electrode are poorly connected and largely isolated from the carbon-based electron-conducting network. In contrast, such inhomogeneous aggregation is not observed in the PW/CNT electrodes. As shown on the left side of the schematic diagram in Fig. 1(a), the Prussian white (PW) and carbon nanotubes were assembled using a conventional slurry process, following our previous report.[23] A mixture of MW-CNTs and SW-CNTs was employed as a conductive binder in place of PVDF. For comparison, control composite electrodes composed of PW, acetylene black, and PVDF binders were also fabricated. It is worth emphasizing that the CNTs network enables stable electrode fabrication on Al@C foil *via* a standard coating process, without the need for polymeric binders.

Electrochemical characteristics: Na$^+$ diffusion dynamics

According to previous reports on the intrinsic properties of Mn-based PBAs, such as Prussian white (PW), high-spin Mn (MnN$_6$) fully participates in redox reactions, contributing significantly to the overall capacity.[22] In contrast, only a limited portion of low-spin Fe (FeC$_6$) engages in redox activity, and compared to an equivalent amount of high-spin Mn, Fe tends to induce more severe lattice distortion.[22] Therefore, activating low-spin Fe within an appropriate voltage range is considered an effective strategy to enhance the electrochemical performance of PBAs. In this study, the initial activation process, performed during the first cycle within a voltage window of 2.0–4.2 V *vs.* Na/Na$^+$, serves as a rapid activation step that facilitates the participation of low-spin Fe in redox reactions.

To ensure efficient electron transport pathways, electrochemical tests were conducted to evaluate the half-cell performance of the as-prepared cathodes incorporating a built-in electron-conducting network. As shown in Fig. 3(a), the PW/
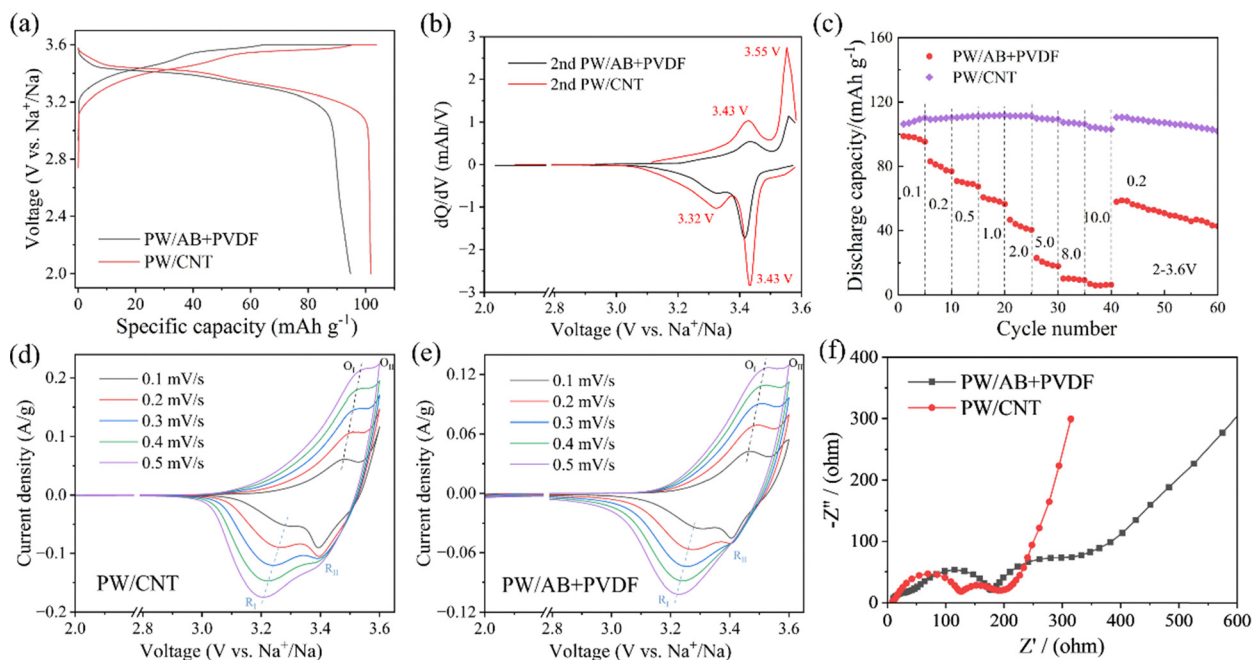
Fig. 3 (a) Typical galvanostatic charge/discharge profiles of PW/CNT and PW/AB+PVDF cathode-based half-cells taken at 0.2C rare. (b) The dQ/dV curves of the as-prepared cathodes after the activation process. (c) Rate performance of the as-prepared cathodes at different C rates. CV curves of (d) PW/CNT-, and (e) PW/AB+PVDF-based cathodes at different scan rates from 0.1 to 0.5 mV s^{-1}. (f) Nyquist plots of PW/CNT-, and PW/AB+PVDF-based cathodes with a controlled SOC of 50%.

CNT cathode delivers a reversible specific discharge capacity of 101.7 mAh g^{-1}, while the PW/AB+PVDF cathode achieves 94.7 mAh g^{-1}. Note that the specific capacities are based on the weight of PW particles in the cathode materials. These results indicate that the 3D CNTs network enables ideal charge/discharge reactions with minimal capacity fading and negligible overpotential caused by internal resistance. Moreover, analysis of the voltage drop at the end of discharge suggests that the cell with the PW/AB+PVDF electrode exhibits higher internal resistance than the one with the PW/CNT electrode. In Fig. 3(b), the dQ/dV curves of the activated PW/CNT cathode reveal two redox couples at 3.43/3.32 and 3.55/3.43 V vs. Na/Na$^+$. Similar redox couples are also observed for the PW/AB+PVDF cathode. However, the PW/CNT electrode shows sharper peaks with smaller potential separations, suggesting that the CNTs network facilitates rapid sodiation/desodiation with lower polarization.

Fig. 3(c) presents the C-rate capability results, where the PW/AB+PVDF cathode shows significant capacity degradation with increasing current density, with the discharge capacity dropping to just 6 mAh g^{-1} at 10C. This performance loss is attributable to microstructural differences stemming from the absence of a robust CNTs network, as discussed earlier (refer to Fig. 2). In contrast, the PW/CNT electrode demonstrates a markedly superior C-rate capability of approximately 103.8 mAh g^{-1} at 10C. Overall, the results in Fig. 2 and 3 clearly demonstrate that the 3D CNTs network in PW/CNT cathodes enhances cell kinetics by promoting efficient electron conduction and ensuring sufficient interfacial contact between the cathode and the electrolyte, thereby enabling excellent high-rate performance.

The Na$^+$ insertion/extraction kinetics and the associated polarization were further investigated using cyclic voltammetry (CV), electrochemical impedance spectroscopy (EIS), and the galvanostatic intermittent titration technique (GITT). The sodium-ion diffusion coefficient (D_{Na}) was calculated based on both anodic and cathodic peak currents at scan rates ranging from 0.1 to 0.5 mV s^{-1}. As shown in Fig. 3(d) and (e), the PW/AB+PVDF electrode exhibits lower current density, broader redox peaks, and a larger peak separation between anodic and cathodic signals in the CV curves, indicating slower sodiation/desodiation kinetics and higher polarization. In contrast, the hybridized 3D CNTs network in the PW/CNT electrode promotes faster Na$^+$ transport with reduced polarization.

Furthermore, in Fig. 3(d) and (e), the redox couple labeled O$_I$/R$_I$ shows increasing polarization at higher scan rates, whereas the O$_{II}$/R$_{II}$ couple exhibits negligible polarization. The redox reaction associated with the low-spin [Fe(CN)$_6$]$^{3-}$/[Fe(CN)$_6$]$^{4-}$ couple demonstrates a faster kinetic response during charge/discharge processes. According to the Randles–Sevcik equation, the peak current (I_p) as a function of the scan rate (ν) can be expressed as follows:

$$I_p = (2.69 \times 10^5) \times \sqrt{n^3} \times A \times \sqrt{D_{Na}} \times C \times \sqrt{V_{rate}} \quad (1)$$

where n is the number of electrons transferred, A is the electrode surface area, D_{Na} is the sodium-ion diffusion coefficient, C is the concentration of the active species, and ν is the scan rate. As shown in Fig. S3(a) and (b), the slope of I_p vs. $V_{rate}^{1/2}$ for the PW/CNT electrode is approximately 3.6 times greater than that for the PW/AB+PVDF electrode.

The corresponding ratio of diffusion coefficients, ($D_{(Na:PW/CNTs)}/D_{(Na:PW/AB+PVDF)}$), is approximately 9:1. This enhanced Na$^+$ diffusion in the PW/CNT cathode supports the observed improvements in battery performance, particularly its superior C-rate capability.

In Fig. 3(f), the Nyquist plots of half-cells aged for one cycle and controlled at a 50% state of charge (SOC) display two semicircles in the high- and medium-frequency regions, along with a sloped line in the low-frequency region. The intercept at high frequency on the real axis (Z') corresponds to the ohmic resistance (R_s). The semicircle in the high-frequency region is attributed to the resistance of the cathode–electrolyte interphase (R_{CEI}), while the semicircle in the medium-frequency region represents the charge transfer resistance (R_{CT}). The sloped line at low frequency corresponds to the Warburg impedance (Z_w), which is associated with Na$^+$ diffusion.[26]

The impedance parameters obtained by fitting the Nyquist plots using an equivalent circuit model are summarized in Table S3, and the circuit model used for fitting is shown in Fig. S4(a). According to the values listed in Table S3, the PW/CNT cell exhibits lower R_s, R_{CEI}, and R_{CT} values compared to the PW/AB+PVDF cell, indicating improved interfacial and charge transfer properties. Na$^+$ diffusion characteristics were further analyzed by examining the linear relationship between the real part of the impedance (Z') and $\omega^{-1/2}$ (the inverse square root of the angular frequency) in the low-frequency region. Using the Warburg impedance coefficient (σ_w), Z' can be expressed as follows:

$$Z' = R_s + R_{ct} + \sigma_w \omega^{-1/2}. \qquad (2)$$

The slope of the Z' vs. $\omega^{-1/2}$ plot corresponds to σ_w. As illustrated in Fig. S4(b), the PW/CNT cell shows a significantly smaller slope than the PW/AB+PVDF cell, indicating faster Na$^+$ diffusion in the PW/CNT electrode.

Next, galvanostatic intermittent titration technique (GITT) measurements were performed to investigate the Na$^+$ diffusion dynamics at the electrode/electrolyte interface. The GITT is a widely used method for determining ion diffusion coefficients from electrochemical data. As shown in Fig. S5(a) and (b), the GITT measurements were carried out by applying continuous galvanostatic pulses at a current rate of 0.1C for 10 minutes, each followed by a rest period of 30 minutes. The sodium-ion diffusion coefficient (D_{Na}) was calculated using the following equation:[27]

$$D_{Na} = \frac{4}{\pi\tau}\left(\frac{nV_m}{S}\right)^2\left(\frac{\Delta E_s}{\Delta E_\tau}\right)^2. \qquad (3)$$

where τ represents the time of the current pulse, n is the number of moles, and V_m is the molar volume of the active material. S denotes the electrode/electrolyte interface area. ΔE_s and ΔE_τ represent the voltage changes during the constant galvanostatic pulse and the steady-state voltage change, respectively. The average Na$^+$ diffusion coefficients of the PW/CNT and PW/AB+PVDF cathodes are calculated as 3.25×10^{-10} and 1.49×10^{-10} cm^2 s^{-1}, respectively. The relatively higher Na$^+$ diffusion coefficient in the PW/CNT cathode can be attributed to the spider-web-like CNTs network embedded within the electrode. This interconnected CNTs structure facilitates rapid electron transport and provides a large specific surface area for electrolyte access, thereby enabling efficient Na$^+$ diffusion through the pores and across the surfaces of the PW particles.

Electrochemical characteristics: cyclability

To evaluate the impact of the three-dimensional CNTs network on the cycling stability of the half-cells, galvanostatic charge/discharge tests were conducted under various conditions. During the initial activation process of the PW/CNT half-cell within a voltage window of 2.0–4.2 V vs. Na/Na$^+$, the cell exhibited an initial charge/discharge specific capacity of 146/137 mAh g^{-1}, corresponding to a relatively high coulombic efficiency (CE) of 94.0%. Fig. 4(a) shows that, after the activation process, the PW/CNT half-cell operating within the voltage range of 2.0–3.6 V exhibits specific charge/discharge capacities of 103.7/101.7 mAh g^{-1}, corresponding to a coulombic efficiency (CE) of 98.1%. The charge/discharge capacity of the PW/CNT half-cell gradually increases up to the 20th cycle and then slowly decreases with further cycling. Remarkably, even after 50 cycles, the specific charge/discharge capacities remain at 104/103 mAh g^{-1}, indicating an excellent capacity retention of 99.3%. This high-capacity retention is attributed to the gradual activation process that follows the initial high-voltage pre-activation. Compared with other reported PW-based cathode materials (Table S4), the PW material in this study demonstrates superior cycling stability within a relatively narrow operating voltage window.

For comparative analysis, a PW/AB+PVDF half-cell was also examined. During the high-voltage pre-activation, this half-cell exhibited specific charge/discharge capacities of 150/129 mAh g^{-1}, corresponding to a coulombic efficiency (CE) of 86.3%. Within a narrower voltage window of 2.0–3.6 V, the PW/AB+PVDF half-cell delivered specific charge/discharge capacities of 97/95 mAh g^{-1}, with a CE of 97.2%, which is slightly lower than that of the PW/CNT half-cell (98.1%). Furthermore, the capacity of the PW/AB+PVDF half-cell continuously declined with cycling. After 50 cycles, it retained specific charge/discharge capacities of only 44/43 mAh g^{-1}, corresponding to a capacity retention of 45%. These results indicate that the PW/AB+PVDF half-cell experiences ongoing side reactions,[23,28] likely triggered by electrolyte decomposition at the electrode–electrolyte interface during repeated cycling. As shown in Fig. S6(a) and S6(b), the polarization of the PW/AB+PVDF electrode increases significantly after the 20th cycle, reflecting a rise in internal impedance. In contrast, the PW/CNT cell exhibits only a slight increase in polarization even after 50 cycles. The observed increase in polarization is primarily attributed to the progressive growth of the cathode–electrolyte interphase (CEI) layer, which is influenced by electrolyte decomposition, interfacial instability, and the structural degradation of the PW powder.

In this context, the 3D CNTs network plays a crucial role not only in enhancing electronic conductivity but also in mitigating structural degradation during high-voltage cycling. The improved
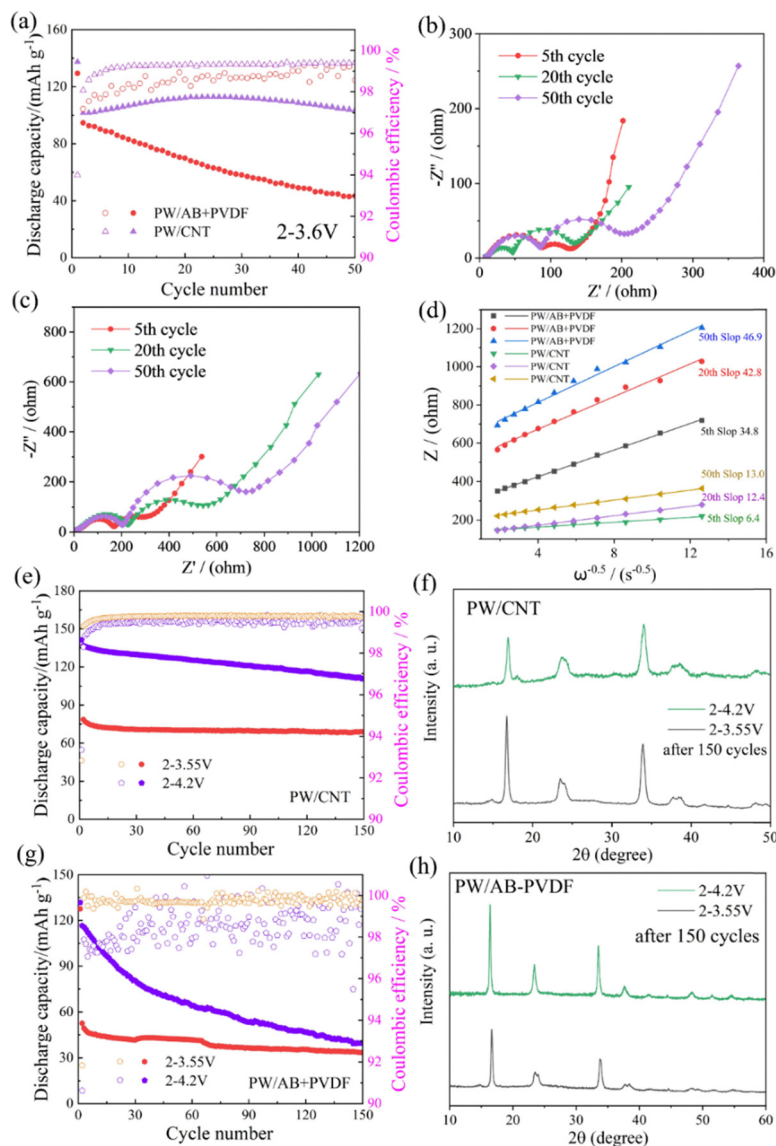
Fig. 4 (a) Cycling performance of the as-prepared cathodes at a current density of 0.2C. *In situ* EIS measurements of (b) PW/CNT- and (c) PW/AB+PVDF-based cathodes at different cycles with a SOC of 50%. (d) Fitted straight lines between Z' and $\omega^{-0.5}$ at the low-frequency for PW/CNT- and PW/AB+PVDF-based cathodes. Cycling performance of (e) PW/CNT- and (g) PW/PVDF-based cathodes at different operating voltage ranges and the same C rate of 1C. XRD patterns of (f) PW/CNT- and (h) PW/AB+PVDF-based cathodes after 150 cycles.

electrical connectivity ensures homogeneous charge distribution and smooth Na$^+$ extraction/insertion kinetics, which suppress localized overpotentials—commonly associated with triggering monoclinic-to-cubic phase transitions in PW. By promoting uniform reaction environments across the electrode, the CNTs framework helps stabilize the monoclinic phase and thereby contributes to the excellent cycling stability observed in the PW/CNT half-cell.

The choice of the MW-CNT/SW-CNT ratio (9 : 1) was based on a balance between the material cost and electrochemical performance observed during preliminary investigations. Given the significantly higher cost and lower availability of SW-CNTs, it is desirable to minimize their use while maintaining sufficient electrical conductivity and mechanical robustness. In the initial screening stage, PW cathodes with MW-CNT/SW-CNT ratios of 100 : 0 (PW97-MW), 90 : 10 (PW98-MW/SW = 90/10),

and 80 : 20 (PW98-MW/SW = 80/20) were fabricated. Notably, the PW98-MW electrode, composed solely of MW-CNTs, failed to form a mechanically robust structure, prompting us to reduce the active material content to 97% to enable proper electrode fabrication.

As shown in Fig. S7, the electrodes with MW-CNT/SW-CNT ratios of 90 : 10 and 80 : 20 exhibited comparable electrochemical performance at 1C within a voltage window of 2.0–4.2 V *vs.* Na/Na$^+$, with the 90 : 10 composition showing slightly better cycling stability. This improvement may be attributed to enhanced network homogeneity at the 90 : 10 ratio, where a small amount of long, flexible SW-CNTs effectively bridges the gaps between MW-CNTs and active material particles, thereby improving both electronic conductivity and structural integrity. In contrast, increasing the SW-CNTs content to 20% (80 : 20)

may promote excessive bundling or agglomeration of SW-CNTs, leading to a less effective conductive network and inferior dispersion, which slightly reduces overall performance. Meanwhile, the electrode composed solely of MW-CNTs (PW97-MW) exhibited significantly inferior electrochemical behaviour, likely due to insufficient inter-tube connectivity and the absence of long-range conductive pathways.

To investigate the underlying mechanism of capacity degradation, *in situ* electrochemical impedance spectroscopy (EIS) measurements were conducted on both PW/CNT and PW/AB+PVDF cells during charge/discharge cycling. As shown in Fig. 4(b) and (c), the Nyquist plots at different cycles with a controlled state of charge (SOC) of 50% display two semicircles in the high- and medium-frequency regions, corresponding to the resistance of the cathode–electrolyte interphase (R_{CEI}) and the charge transfer resistance (R_{CT}), respectively. Both PW/CNT and PW/AB+PVDF cells exhibit a similar trend of impedance evolution: R_{CEI} and R_{CT} initially decrease, indicating electrode activation, and then increase in the later cycles, suggesting structural degradation of the PW lattice and excessive growth of the CEI layer. Notably, the PW/CNT cell exhibits smaller fluctuations in R_{CEI} and R_{CT}, implying better interfacial and structural stability. Fig. 4(d) presents linear fits between the real part of the impedance (Z') and $\omega^{-1/2}$, which show an initial decrease in slope followed by an increase with continued cycling. This trend is consistent with the evolution of the impedance parameters. Importantly, the slopes for the PW/CNT cell remain significantly smaller than those of the PW/AB+PVDF cell across all cycles, indicating that Na$^+$ diffusion in the PW/CNT electrode is less affected by CEI formation and structural degradation.

To investigate the structural changes of PW particles in the electrodes after 150 cycles, *ex situ* X-ray diffraction (XRD) measurements were performed. Initially, a high-voltage pre-activation step was conducted at 0.2C within a voltage range of 2.0–4.2 V, followed by cycling in the designated operating voltage windows at a current density of 1C. As shown in Fig. 4(e), the PW/CNT half-cell exhibits gradual capacity decay in the 2.0–4.2 V range while still retaining a reversible specific capacity of 111 mAh g^{-1} after 150 cycles. In contrast, when operated in the narrower voltage window of 2.0–3.55 V, the PW/CNT half-cell shows negligible capacity loss even after 150 cycles. Fig. 4(f) presents the *ex situ* XRD patterns of PW/CNT cathodes obtained from half-cells aged over 150 cycles at different operating voltages. The diffraction peaks are predominantly associated with the monoclinic phase of PW, indicating minimal phase transition to the cubic phase. In particular, the XRD pattern of the PW/CNT cathode cycled between 2.0 and 4.2 V shows relatively broader and weaker peaks, which can be attributed to the formation of a thicker cathode–electrolyte interphase (CEI) layer caused by increased side reactions at higher voltages. In contrast, as illustrated in Fig. 4(g), the PW/AB+PVDF half-cell demonstrates rapid capacity degradation in the 2.0–4.2 V range, with charge/discharge capacities declining to 40/40 mAh g^{-1} after 150 cycles. Although improved capacity retention is observed in the narrower 2.0–3.55 V window, the

PW/AB+PVDF half-cell still exhibits a relatively low reversible capacity of 32 mAh g^{-1} after 150 cycles. Fig. 4(h) shows the XRD patterns of PW/AB+PVDF cathodes after 150 cycles under different operating voltages. The cathode cycled in the 2.0–3.55 V range displays intense peaks corresponding to the monoclinic PW phase. However, the cathode cycled in the 2.0–4.2 V range reveals a distinct sharp peak corresponding to the cubic phase of PW, indicating an irreversible phase transition. Similar structural degradation phenomena have been reported in previous studies of deteriorated PW systems.[29]

To further investigate the structural characteristics of the electrodes and evaluate their surface chemical stability, field-emission scanning electron microscopy (FE-SEM) imaging and X-ray photoelectron spectroscopy (XPS) measurements were conducted on electrodes harvested from cycled half-cells. As shown in Fig. 5(a) and (b), the CNTs network on the surface of the PW/CNT cathode remains firmly attached to the PW particles, preserving the structural integrity of the active material. This demonstrated that structural stability can be attributed to the three-dimensionally interconnected CNTs network. Moreover, the robust conductive framework provided by the CNTs binder is expected to promote homogenization of the electrochemical reactions within the porous architecture of the PW/CNT electrode. The porous nature of the electrode also accommodates the volume changes of PW particles during charge/discharge processes. The 3D microstructure enables elastic expansion and contraction, maintaining the mechanical and electrochemical integrity of the composite electrode. In contrast, as shown in Fig. 5(c) and (d), multiple cracks are observed on the PW particles in the PW/AB+PVDF electrode after 150 cycles. The formation of microcracks during cycling disrupts the conductive network, resulting in inhomogeneous Na$^+$ insertion/extraction, uneven electrochemical reactions, phase transitions, and side reactions such as excessive CEI growth and transition metal dissolution into the electrolyte.[30,31] In conclusion, the intact 3D CNTs network plays a crucial role in maintaining structural stability and enhancing electrochemical performance, making PW-based composite electrodes with CNTs binders highly suitable for sodium-ion battery applications.

To investigate the structural evolution during cycling, operando X-ray diffraction (XRD) measurements were conducted using specially assembled *in situ* cells with PW/CNT- and PW/AB+PVDF-based cathodes. The measurements were performed under two voltage conditions: the activation window (2.0–4.2 V (*vs.* Na/Na$^+$), first cycle) and the working voltage window (2.0–3.6 V (*vs.* Na/Na$^+$), third cycle). As shown in Fig. 6(a), for the PW/CNT-based cathode cycled within 2.0–4.2 V, the left-side peak splitting around 24° and 38° gradually intensify and then diminish during charging. A similar trend is observed during discharging, with the peaks returning to their initial state, indicating that the monoclinic phase of PW is retained throughout the cycle without a significant phase transformation. In contrast, as shown in Fig. S8(a), the PW/AB+PVDF-based cathode displays markedly different behaviours. The splitting peaks near 24° and 38° nearly disappear upon charging to 4.2 V and reappear upon discharging, signifying a reversible monoclinic-
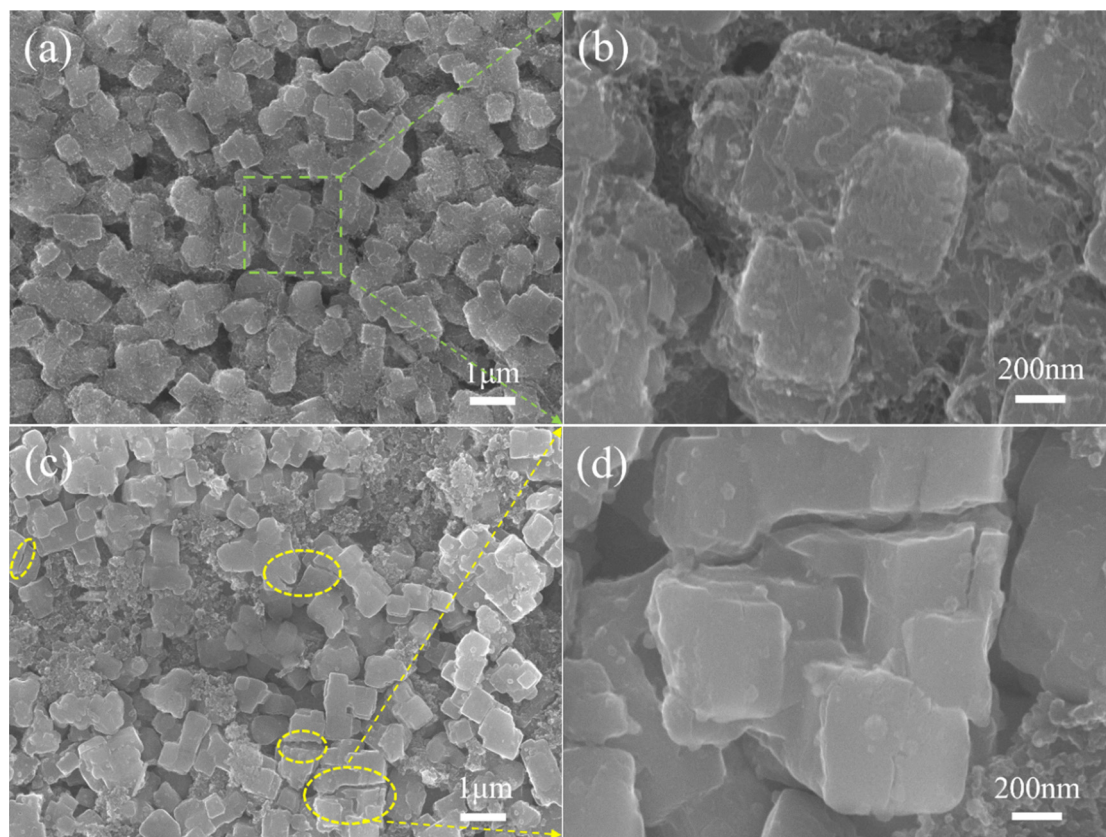
Fig. 5 FE–SEM images of (a) and (b) PW/CNT– and (c) and (d) PW/AB+PVDF–based 150 cycled electrodes.

to-cubic phase transition under high-voltage cycling. Additionally, during the first-cycle activation process (2.0–4.2 V), both cathodes exhibit a reversible shift in the diffraction peaks near 34°. These previously split peaks merge into a broader single peak upon charging and do not fully recover after discharging, though the 2θ position shifts reversibly. These features reflect reversible lattice parameter changes, indicative of lattice expansion/contraction and a reduction in crystallinity. Under the narrower voltage window of 2.0–3.6 V, as shown in Fig. 6(b) and Fig. S8(b), both electrodes exhibit only periodic modulation of the peak intensities near 24° and 38°, along with reversible peak shifts near 34° during charge/discharge cycles. These results suggest that PW undergoes a solid-solution reaction mechanism in this voltage range, which is critical to the excellent cycling stability observed under these conditions. In summary, the 3D-interconnected CNTs network in the PW/CNT-based cathode not only provides an efficient electronic conduction pathway but also facilitates uniform electron and ion transport. This conductive framework buffers the volume changes of PW during cycling and mitigates the stress concentration, thereby effectively suppressing severe lattice reconstruction.[32,33] In contrast, the PW/AB+PVDF-based cathode lacks such structural reinforcement, leading to greater fluctuations in local Na$^+$ concentrations and the accumulation of mechanical stress, ultimately resulting in increased structural degradation and particle fracture over long-term cycling.

The cycling performance of a full cell was evaluated over 20 cycles at a 1C rate, using a configuration denoted as the hard carbon-CNT| PW-CNT for confirming its feasibility as a cathode for SIBs. As shown in Fig. S9, the full cell demonstrated an initial discharge capacity of 98.1 mAh g^{-1} and a coulombic efficiency of 69.3% at 0.2C. While the capacity was gradually degraded to 71.14 mAh g^{-1} at the initial stage of cycles, it tended to stabilize at certain levels. The relatively low initial coulombic efficiency is primarily attributed to irreversible Na$^+$ consumption at the hard carbon anode, a common issue in sodium-ion full cells. This loss is mainly due to solid electrolyte interphase (SEI) formation on the HC surface during the initial sodiation, which irreversibly consumes Na$^+$. In particular, the high surface area and internal porosity of the HC used in this study likely exacerbate electrolyte decomposition and SEI growth, thereby lowering the first-cycle efficiency. Since observed low first coulombic efficiency and the good structural stability of the PW/CNT cathode confirmed by half-cell tests, the dominant factor in capacity loss involves the side reactions at the hard carbon anode surface and/or in nanopores in association with irreversible Na$^+$ loss for making excess solid electrolyte interface layer formation. Further optimization of the hard carbon-CNT anode is currently underway, and it is highly possible to further improve the cycle characteristics by optimizing the electrolytes and additives.

Surface chemical states and oxidation states of transition metals in PW particles

To further elucidate the origin of the excellent electrochemical performance exhibited by the PW/CNT cathodes, X-ray
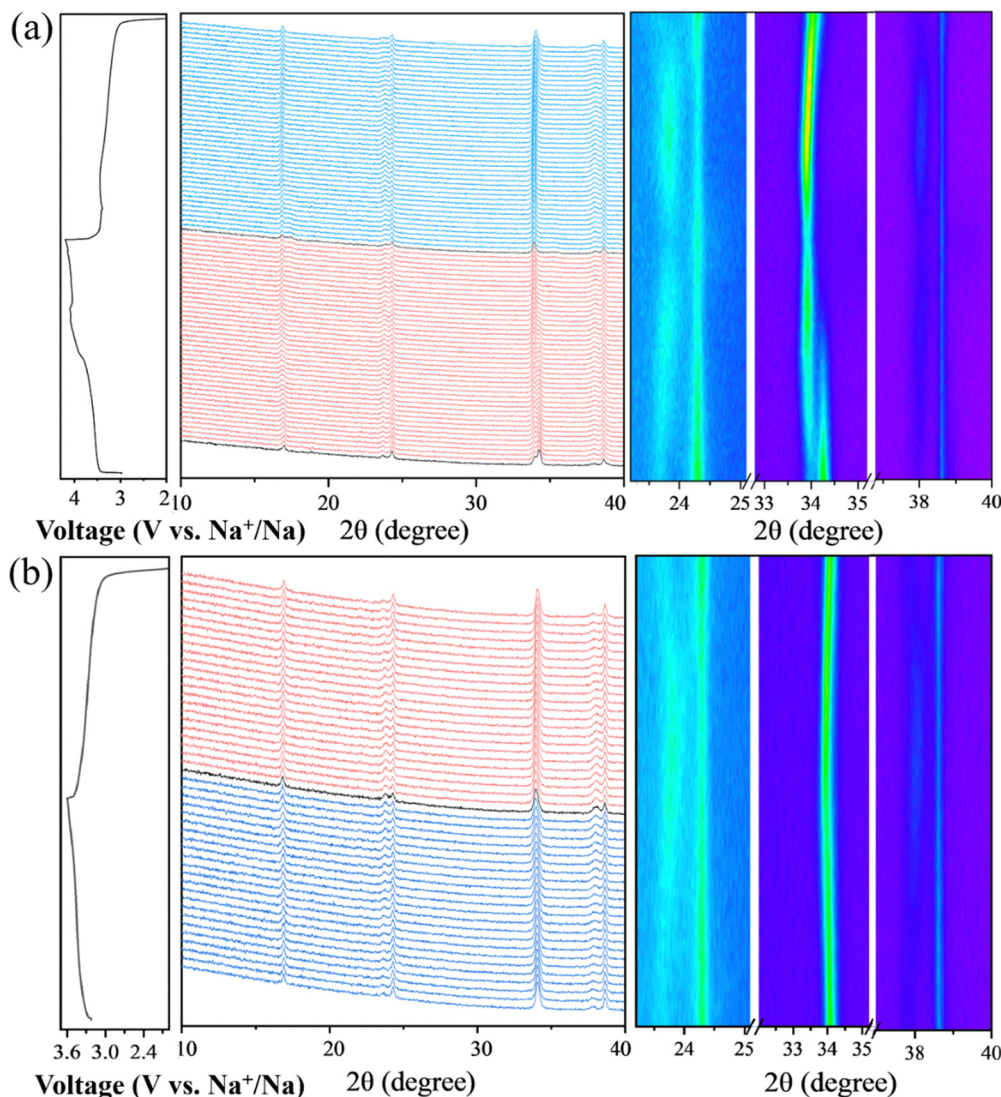
Fig. 6 The operando XRD measurements of the PW/CNT-based cathode at different operating voltages (a) 2–4.2 V for the first cycle and (b) 2–3.6 V for the third cycle.

photoelectron spectroscopy (XPS) was conducted to examine the surface chemistry and valence states of the electrode materials. In the Fe 2p core-level spectrum (Fig. 7(a)), peaks at 708.8 eV and 721.7 eV correspond to Fe $2p_{3/2}$ and Fe $2p_{1/2}$, respectively, and are characteristic of the Fe(II) oxidation state.[34,35] Notably, no significant changes are observed in the Fe 2p spectrum after electrode activation, indicating the chemical stability of Fe under the tested conditions. In the Mn 2p core-level spectrum (Fig. 7(b)), the Mn $2p_{3/2}$ peaks at 642.1 eV and 643.8 eV, and the Mn $2p_{1/2}$ peaks at 654.0 eV and 655.2 eV, are attributed to Mn(II) and Mn(III) oxidation states, respectively.[36,37] An increase in the area under the Mn(III)-related peaks after activation suggests the occurrence of partial irreversible oxidation reactions, potentially associated with structural changes in the PW lattice. The increase in Jahn–Teller-distorted Mn^{3+} ions within the PW structure during activation likely induces local lattice strain, which may contribute to performance degradation if not effectively mitigated. However, in the PW/CNT system, the 3D CNTs network likely buffers such strain, supporting enhanced structural and electrochemical stability.

Regarding the interface between PW and CNTs, we did not observe direct evidence of chemical bonding (e.g., C≡N–Fe) in our characterization. The XPS spectra of the composite did not show any new peaks or shifts indicative of covalent bond formation between the components. However, the uniform coating of CNTs on the PW surface and the overall improved electronic conductivity suggest a strong physical interaction, such as van der Waals forces and mechanical entanglement. This physical integration ensures tight interfacial contact and efficient electron transport, contributing significantly to the excellent electrochemical performance, as evidenced by the enhanced rate capability and cycling stability.

The C 1s core-level spectrum of the one cycle-aged PW/CNT electrode, as illustrated in Fig. 7(c), consists of four components with binding energies of 284.8 eV (C–C), 285.6 eV (C–O/C–N), 287.4 eV (COO), and 290.6 eV (O–C(=O)–O).[38] A new XPS
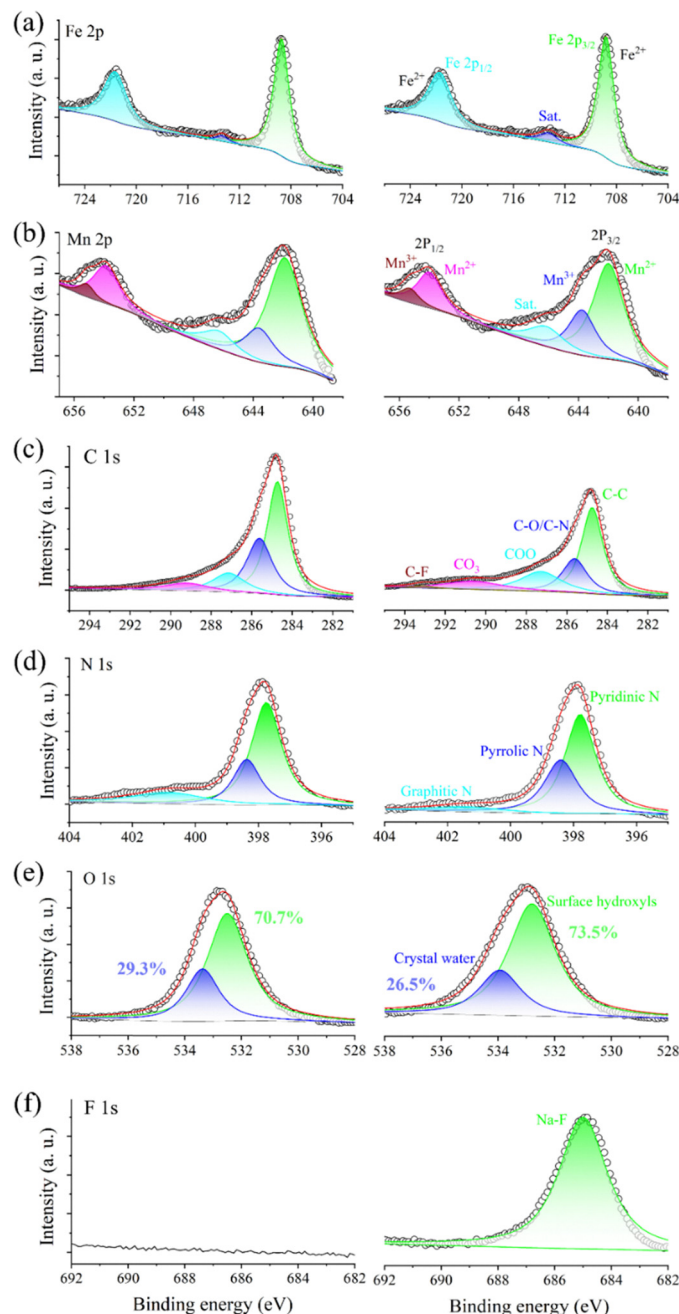
Fig. 7 XPS analysis of the PW/CNT-based cathode in the (a) Fe 2p, (b) Mn 2p, (c) C 1s, (d) N 1s, (e) O 1s, and (f) F 1s before and after activation.

peak at 293.0 eV (C–F) observed after activation of the PW/CNT electrode indicates the presence of fluorinated organic species that are formed after oxidative decomposition of fluoroethylene carbonate (FEC) in the CEI layer.[39,40] In the N 1s core-level spectrum (Fig. 7(d)), peaks at 397.8, 398.4, and 401.4 eV correspond to pyridinic, pyrrolic, and graphitic nitrogen species, respectively. Note that similar spectroscopic characteristics were observed for the PW/AB+PVDF electrodes (Fig. S10(a)–(d)).

The O 1s core-level spectrum of the PW/CNT cathode, as shown in Fig. 7(e), exhibits two distinct peaks at 532.8 and 533.9 eV, which are attributed to surface hydroxyl groups and crystal water, respectively.[41,42] Following the activation process,

no significant changes were observed in the intensity or width of these peaks, indicating the chemical stability of oxygen species in the PW/CNT electrode. In contrast, substantial changes were observed in the O 1s spectrum of the PW/AB+PVDF cathode after activation (Fig. S10(e)). Specifically, activation led to a reduction and narrowing of the peak associated with surface hydroxyls and a corresponding increase and broadening of the peak associated with crystal water. These changes suggest that water molecules initially present on the electrode surface may have migrated into the PW crystal lattice, resulting in the formation of interstitial water. Surface water in composite electrodes can primarily originate from two sources:

(i) minor surface adsorption during sample transfer and handling and (ii) water generation *via* decomposition of the cathode–electrolyte interphase (CEI).[43] The CNT-based conductive network is effective in suppressing both water adsorption and migration by maintaining a stable interfacial structure, thereby mitigating side reactions involving water and reducing the risk of transition metal dissolution in the PW cathode.[44] In Fig. 7(f), a new peak appears at 685.0 eV in the F 1s core-level spectrum of the PW/CNT cathode after activation. This peak is indicative of NaF formation within the cathode–electrolyte interphase (CEI) layer on the surface of the PW particles.[45] In contrast, the F 1s spectrum of the PW/AB+PVDF cathode before activation, as shown in Fig. S10(f), displays only a single peak at 687.9 eV, which corresponds to the CF_2 groups from the PVDF binder.[46] After activation, the F 1s spectrum of the PW/AB+PVDF cathode exhibits two peaks: one at 687.9 eV (CF_2-related) and another at 685.0 eV (NaF-related), indicating the formation of NaF during cycling. Compared with the PW/AB+PVDF cathode, the PW/CNT cathode exhibits the formation of a denser NaF-rich CEI layer. This denser CEI layer helps both Na^+ ion diffusion at near the PW particle surface due to its higher Na^+ conductivity and suppress excess electrolyte decomposition, thereby contributing to improved interfacial stability and electrochemical performance.[47] This is consistent with the impedance measurement results, as shown in Fig. 3(f).

Conclusions

An ultra-high content ($>$98 wt%) PW cathode was achieved through the self-assembly of a homogeneous three-dimensional (3D) carbon nanotubes (CNTs) network. By hybridizing multi-walled carbon nanotubes (MW-CNTs) with a small amount of single-walled carbon nanotubes (SW-CNTs) in an optimized ratio, the PW/CNT cathode demonstrated enhanced C-rate capability and improved long-term cycling stability, eliminating the need for polymeric binders. Systematic investigations were carried out to characterize the structural features of the composite electrodes. CNTs adsorbed on the surface of PW particles were spontaneously incorporated into the intergranular nanospaces, facilitating effective interparticle bridging within the PW/CNT architecture. This study demonstrates that 3D grid-like CNTs network uniformly distributed across the electrode surface enhance electron transport and ensure sufficient interfacial contact with the electrolyte. Moreover, the intrinsic elasticity of CNTs is considered to help maintain the mechanical integrity of the electrode structure. The 3D interconnected CNTs framework, which encapsulates the active material, enables elastic expansion and contraction during charge/discharge cycles, thereby mitigating the mechanical stress caused by volumetric changes in PW particles. Furthermore, this structure effectively suppresses crack formation and prevents undesirable irreversible phase transitions under high operating voltages, thereby improving electrode stability and performance. The material design strategy proposed in this work offers a promising approach for enhancing the energy density of SIBs while simultaneously achieving high-rate capability and cycle life. This strategy may serve as a viable pathway for developing next-generation cathode materials aimed at enabling extended driving ranges (*e.g.*, $\sim$250 km per charge) for electric vehicles (EVs).

Author contributions

Nobuyuki Zettsu (N. Z.) conceived the study. Yang He (Y. H.) and Tingru Chen (T. C.) performed the preparation and electrochemical characterization experiments. N. Z. and Y. H. wrote the manuscript.

Conflicts of interest

There are no conflicts to declare.

Data availability

The authors confirm that the data supporting the findings of this study are available within the article and its SI. The Supplementary Information provides additional experimental data and analyses, including violin plots of multiprobe surface potential measurements, morphological characterizations, electrochemical kinetics and impedance analyses, Na diffusion behavior, operando XRD, and XPS studies. It also contains detailed charge/discharge profiles, cycling performance of different electrode compositions, as well as quantitative elemental table supporting the main text. See DOI: **https://doi.org/10.1039/d5ma00698h**

Acknowledgements

Notes and references

1 J. Hjalmarsson, K. Thomas and C. Boström, *J. Energy Storage*, 2023, **60**, 106639.

2 Y. Song, L. Wang, L. Sheng, D. Ren, H. Liang, Y. Li, A. Wang, H. Zhang, H. Xu and X. He, *Energy Environ. Sci.*, 2023, **16**, 1943–1963.

3 Z. Li, L. Wang, X. Huang and X. He, *Small*, 2024, **20**, 2305429.

4 Y. He, C. Liu, Z. Xie, P. Xiaokaiti, G. Chen, Z. Feng, Y. Kasai, A. Abudula and G. Guan, *Adv. Compos. Hybrid Mater.*, 2023, **6**, 85.

5 Y. He, C. Liu, S. Peng, J. Zhang, G. Chen, Z. Feng, Q. Zhao, A. Abudula and G. Guan, *J. Mater. Sci. Technol.*, 2023, **145**, 210–220.

6 J. Liu, Y. Wang, N. Jiang, B. Wen, C. Yang and Y. Liu, *Angew. Chem., Int. Ed.*, 2024, **63**, e202400214.

7 J.-H. Lee, J.-G. Bae, M. S. Kim, J. Y. Heo, H. J. Lee and J. H. Lee, *ACS Nano*, 2024, **18**, 1995–2005.

8 Y. Fang, L. Xiao, Z. Chen, X. Ai, Y. Cao and H. Yang, *Electrochem. Energy Rev.*, 2018, **1**, 294–323.

9 T. Zhang, M. Ren, Y. Huang, F. Li, W. Hua, S. Indris and F. Li, *Angew. Chem., Int. Ed.*, 2024, **63**, e202316949.

10 X. Lu, S. Li, Y. Li, F. Wu, C. Wu and Y. Bai, *Adv. Mater.*, 2024, **36**, 2407359.

11 Y. Yao, M. Pei, C. Su, X. Jin, Y. Qu, Z. Song, W. Jiang, X. Jian and F. Hu, *Small*, 2024, **20**, 2401481.

12 F. Peng, L. Yu, P. Gao, X.-Z. Liao, J. Wen, Y.-S. He, G. Tan, Y. Ren and Z.-F. Ma, *J. Mater. Chem. A*, 2019, **7**, 22248–22256.

13 Y. Zhao, J. Peng, K. Chen, L. Luo, H. Chen, H. Zhang, S. Chou, X. Feng, W. Chen, R. Cao, X. Ai, Y. Fang and Y. Cao, *Sci. China: Chem.*, 2023, **66**, 3154–3160.

14 X. Jian, X. Liu, C. Yang, J. Xie, W. Hu, Y. Zhang, H. Yan, J. Han and Y. You, *Small*, 2024, **20**, 2400709.

15 J. Lee, W. Jeong, J. Baek, Y. Kim, Y. Choi, V. Mathew, B. Sambandam, M. H. Alfaruqi and J. Kim, *J. Mater. Chem. A*, 2023, **11**, 25724–25733.

16 Y. Shang, B. Ren, R. Wu, J. Lin, X. Li, J. Shen, D. Yan and H. Y. Yang, *Small*, 2024, **21**, 2408018.

17 H. Fu, M. Xia, R. Qi, X. Liang, M. Zhao, Z. Zhang, X. Lu and G. Cao, *J. Power Sources*, 2018, **399**, 42–48.

18 Y. Tang, W. Li, P. Y. Feng, M. Zhou, K. L. Wang, Y. S. Wang, K. R. Zaghib and K. Jiang, *Adv. Funct. Mater.*, 2020, **30**, 1908754.

19 Y. Liu, D. He, Y. Cheng, L. Li, Z. Lu, R. Liang, Y. Fan, Y. Qiao and S. Chou, *Small*, 2020, **16**, 1906946.

20 Y. luo, L. Yang, Q. Liu and Y. Yan, *R. Soc. Open Sci.*, 2021, **8**, 211092.

21 Y. He, S. L. Dreyer, T. Akçay, T. Diemant, R. Mönig, Y. Ma, Y. Tang, H. Wang, J. Lin, S. Schweidler, M. Fichtner, H. Hahn, T. Brezesinski, B. Breitung and Y. Ma, *ACS Nano*, 2024, **18**, 24441–24457.

22 Z. Wang, M. T. Sougrati, Y. He, P. N. Le Pham, W. Xu, A. Iadecola, R. Ge, W. Zhou, Q. Zheng, X. Li and J. Wang, *Nano Energy*, 2023, **109**, 108256.

23 D.-w Kim, N. Zettsu and K. Teshima, *J. Mater. Chem. A*, 2019, **7**, 17412–17419.

24 A. Paolella, C. Faure, V. Timoshevskii, S. Marras, G. Bertoni, A. Guerfi, A. Vijh, M. Armand and K. Zaghib, *J. Mater. Chem. A*, 2017, **5**, 18919–18932.

25 W. Wang, Y. Gang, Z. Hu, Z. Yan, W. Li, Y. Li, Q. F. Gu, Z. Wang, S. L. Chou, H. K. Liu and S. X. Dou, *Nat. Commun.*, 2020, **11**, 980.

26 L. Li, P. Nie, Y. Chen and J. Wang, *J. Mater. Chem. A*, 2019, **7**, 12134–12144.

27 Y. He, C. Liu, Z. Xie, J. Wang, G. Chen, Q. Zhao, A. Abudula and G. Guan, *ACS Appl. Energy Mater.*, 2022, **5**, 8697–8708.

28 J. Xia, K. J. Nelson, Z. Lu and J. R. Dahn, *J. Power Sources*, 2016, **329**, 387–397.

29 L. Shen, Y. Jiang, Y. Liu, J. Ma, T. Sun and N. Zhu, *Chem. Eng. J.*, 2020, **388**, 124228.

30 F. Wu, A. Mullaliu, T. Diemant, D. Stepien, T. N. Parac-Vogt, J.-K. Kim, D. Bresser, G.-T. Kim and S. Passerini, *InfoMat*, 2023, **5**, e12462.

31 U.-H. Kim, L.-Y. Kuo, P. Kaghazchi, C. S. Yoon and Y. K. Sun, *ACS Energy Lett.*, 2019, **4**, 576–582.

32 T. Jin, Q. Han and L. Jiao, *Adv. Mater.*, 2020, **32**, 1806304.

33 P. Wan, H. Xie, N. Zhang, S. Zhu, C. Wang, Z. Yu, W. Chu, L. Song and S. Wei, *Adv. Funct. Mater.*, 2020, **30**, 2002624.

34 Y. Wang, N. Jiang, J. Liu, S. Sun, X. Wang, J. Yang, C. Yang and Y. Liu, *Adv. Funct. Mater.*, 2024, **34**, 2406809.

35 P.-F. Wang, T. Jin, J. Zhang, Q.-C. Wang, X. Ji, C. Cui, N. Piao, S. Liu, J. Xu, X.-Q. Yang and C. Wang, *Nano Energy*, 2020, **77**, 105167.

36 J. Dai, S. Tan, L. Wang, F. Ling, F. Duan, M. Ma, Y. Shao, X. Rui, Y. Yao, E. Hu, X. Wu, C. Li and Y. Yu, *ACS Nano*, 2023, **17**, 20949–20961.

37 Y. Liu, D. He, R. Han, G. Wei and Y. Qiao, *Chem. Commun.*, 2017, **53**, 5569–5572.

38 R. Marrache, T. Mukra, P. Shekhter and E. Peled, *J. Solid State Electrochem.*, 2022, **26**, 2027–2038.

39 M. Ma, H. Cai, C. Xu, R. Huang, S. Wang, H. Pan and Y.-S. Hu, *Adv. Funct. Mater.*, 2021, **31**, 2100278.

40 L. Zhou, Z. Cao, J. Zhang, Q. Sun, Y. Wu, W. Wahyudi, J.-Y. Hwang, L. Wang, L. Cavallo, Y.-K. Sun, H. N. Alshareef and J. Ming, *Nano Lett.*, 2020, **20**, 3247–3254.

41 D. O. Ojwang, M. Svensson, C. Njel, R. Mogensen, A. S. Menon, T. Ericsson, L. Häggström, J. Maibach and W. R. Brant, *ACS Appl. Mater. Interfaces*, 2021, **13**, 10054–10063.

42 W. Wang, Y. Gang, J. Peng, Z. Hu, Z. Yan, W. Lai, Y. Zhu, D. Appadoo, M. Ye, Y. Cao, Q.-F. Gu, H.-K. Liu, S.-X. Dou and S.-L. Chou, *Adv. Funct. Mater.*, 2022, **32**, 2111727.

43 G. G. Eshetu, T. Diemant, M. Hekmatfar, S. Grugeon, R. J. Behm, S. Laruelle, M. Armand and S. Passerini, *Nano Energy*, 2019, **55**, 327–340.

44 W. Guo, W. Wei, H. Zhu, Y. Hu, H. Jiang and C. Li, *eScience*, 2023, **3**, 100082.

45 H. Lohani, D. T. Duncan, X. Qin, P. Kumari, M. Kar, A. Sengupta, A. Ahuja, A. Bhowmik and S. Mitra, *Small*, 2024, **20**, e2311157.

46 B. Xie, L. Wang, H. Li, H. Huo, C. Cui, B. Sun, Y. Ma, J. Wang, G. Yin and P. Zuo, *Energy Storage Mater.*, 2021, **36**, 99–107.

47 M. Ye, S. You, J. Xiong, Y. Yang, Y. Zhang and C. C. Li, *Mater. Today Energy*, 2022, **23**, 100898.